

Research Paper

Ultrasound molecular imaging as a non-invasive companion diagnostic for netrin-1 interference therapy in breast cancer

Jennifer Wischhusen^{1,2,3}, Katheryne E. Wilson², Jean-Guy Delcros³, Rodolfo Molina-Peña¹, Benjamin Gibert³, Shan Jiang³, Jacqueline Ngo¹, David Goldschneider⁴, Patrick Mehlen^{3,4*}, Juergen K. Willmann^{2*†}, Frederic Padilla^{1✉*}

1. Univ Lyon, Université Lyon 1, Centre Léon Bérard, INSERM, LabTAU, F-69003, LYON, France.
2. Department of Radiology, School of Medicine, Stanford University, 94305 Stanford, USA.
3. Apoptosis, Cancer and Development Laboratory – Equipe labellisée ‘La Ligue’, LabEx DEVweCAN, Centre de Cancérologie de Lyon, INSERM U1052-CNRS UMR5286, Centre Léon Bérard, 69008 Lyon, France ;
4. Netris Pharma, 69008 Lyon, France.

*P. Mehlen, J. K. Willmann and F. Padilla contributed equally as senior authors of this article.

†deceased on January 8, 2018

✉ Corresponding author: Dr. Frederic Padilla. LabTAU INSERM U1032, 151 cours Albert Thomas, 69003 Lyon. Mobile: +33 778210650; e-mail: Frederic.Padilla@inserm.fr

© Ivyspring International Publisher. This is an open access article distributed under the terms of the Creative Commons Attribution (CC BY-NC) license (<https://creativecommons.org/licenses/by-nc/4.0/>). See <http://ivyspring.com/terms> for full terms and conditions.

Received: 2018.05.12; Accepted: 2018.07.24; Published: 2018.10.06

Abstract

In ultrasound molecular imaging (USMI), ligand-functionalized microbubbles (MBs) are used to visualize vascular endothelial targets. Netrin-1 is upregulated in 60% of metastatic breast cancers and promotes tumor progression. A novel netrin-1 interference therapy requires the assessment of netrin-1 expression prior to treatment. In this study, we studied netrin-1 as a target for USMI and its potential as a companion diagnostic in breast cancer models.

Methods: To verify netrin-1 expression and localization, an *in vivo* immuno-localization approach was applied, in which anti-netrin-1 antibody was injected into living mice 24 h before tumor collection, and revealed with secondary fluorescent antibody for immunofluorescence analysis. Netrin-1 interactions with the cell surface were studied by flow cytometry. Netrin-1-targeted MBs were prepared using MicroMarker Target-Ready (VisualSonics), and validated in *in vitro* binding assays in static conditions or in a flow chamber using purified netrin-1 protein or netrin-1-expressing cancer cells. *In vivo* USMI of netrin-1 was validated in nude mice bearing human netrin-1-positive SKBR7 tumors or weakly netrin-1-expressing MDA-MB-231 tumors using the Vevo 2100 small animal imaging device (VisualSonics). USMI feasibility was further tested in transgenic murine FVB/N Tg(MMTV/PyMT634Mul) (MMTV-PyMT) mammary tumors.

Results: Netrin-1 co-localized with endothelial CD31 in netrin-1-positive breast tumors. Netrin-1 binding to the surface of endothelial HUVEC and cancer cells was partially mediated by heparan sulfate proteoglycans. MBs targeted with humanized monoclonal anti-netrin-1 antibody bound to netrin-1-expressing cancer cells in static and dynamic conditions. USMI signal was significantly increased with anti-netrin-1 MBs in human SKBR7 breast tumors and transgenic murine MMTV-PyMT mammary tumors compared to signals recorded with either isotype control MBs or after blocking of netrin-1 with humanized monoclonal anti-netrin-1 antibody. In weakly netrin-1-expressing human tumors and normal mammary glands, no difference in imaging signal was observed with anti-netrin-1- and isotype control MBs. *Ex vivo* analysis confirmed netrin-1 expression in MMTV-PyMT tumors.

Conclusions: These results show that USMI allowed reliable detection of netrin-1 on the endothelium of netrin-1-positive human and murine tumors. Significant differences in USMI signal for netrin-1 reflected the significant differences in netrin-1 mRNA & protein expression observed between different breast tumor models. The imaging approach was non-invasive and safe, and provided the netrin-1 expression status in near real-time. Thus, USMI of netrin-1 has the potential to become a companion diagnostic for the stratification of patients for netrin-1 interference therapy in future clinical trials.

Key words: ultrasound molecular imaging, netrin-1, companion diagnostic, breast cancer, targeted microbubbles

Introduction

Netrin-1 is a laminin-related protein involved in axon outgrowth and tumorigenesis [1–4]. Netrin-1 was shown to be overexpressed in 60% of metastatic breast cancers [5]. Following extensive preclinical studies [6,7], a novel therapeutic approach based on netrin-1 interference recently entered a Phase 1 clinical trial to evaluate safety, pharmacokinetics, and clinical activity of a humanized monoclonal antibody targeting netrin-1 (NET1-H-mAb, NP137, Netris Pharma, Lyon, France) in patients with advanced solid tumors (NCT02977195). A companion diagnostic is now required for patient stratification. Although netrin-1 is a secreted protein, its detection in blood serum samples is not feasible. To avoid invasive biopsy-based techniques, a non-invasive molecular imaging approach was developed. As netrin-1 is expressed on endothelial cells interacting among others with CD146 [8–11], we hypothesized that netrin-1-overexpressing tumors might present netrin-1 specifically on the tumor endothelium, providing the opportunity to develop an intravascular molecular imaging approach.

Ultrasound molecular imaging (USMI) can provide a non-invasive, cost-effective, image-based companion diagnostic for the novel netrin-1 interference therapy, as it combines the advantages of ultrasound, such as real-time anatomical imaging, with the capabilities of molecular imaging, such as high sensitivity and specificity *in vivo*. Anatomical and functional ultrasound imaging are integral parts of clinical breast cancer screening and diagnosis complementing mammography, guiding core needle biopsies, and detecting abdominal metastases for the management of breast cancer [12]. Though, ultrasound imaging is limited to soft tissues and cannot be applied to bone or lung metastases. Ultrasound imaging has become molecularly specific with the development of ultrasound contrast agents (UCAs) targeted with ligands such as antibodies or other proteins to detect expression of cancer-specific molecular markers on the vascular endothelium [13–15], such as CD276 (or B7-H3) in ovarian and breast cancer, or secreted frizzled related protein 2 in angiosarcoma [16–22], to allow cancer early detection,

prediction of therapy response, and treatment follow-up [23–29]. Recent clinical demonstration of feasibility and safety of VEGFR2 imaging in breast, ovarian, and prostate cancer patients with the first clinical grade UCA (BR55) has opened the way for further clinical translations of USMI [30,31]. Our objective was to extend USMI to the novel cancer biomarker netrin-1 with the purpose of developing a unique, non-invasive approach to detect netrin-1 overexpression in breast cancer, eventually enabling patient-based treatment decisions.

Here we report the vascular presentation of netrin-1 by endothelial cells *in vivo* in netrin-1-positive breast tumor models and show the feasibility of ultrasound molecular imaging of netrin-1 to discriminate between strongly and weakly netrin-1-expressing tumors. We showed that (**Figure 1**): A) netrin-1 was presented by endothelial cells as assessed by *in vivo* immuno-localization; B) netrin-1-targeted microbubbles selectively bound to netrin-1 protein and netrin-1-presenting cells *in vitro*; C) *in vivo* imaging of netrin-1 revealed significantly enhanced signal with netrin-1-targeted MBs compared with isotype control MBs in nude mice bearing human strongly netrin-1-positive SKBR7 breast tumors and in transgenic mice developing spontaneous mammary adenocarcinoma (MMTV-PyMT), while there was no significant difference between targeted and control contrast agents in nude mice bearing weakly netrin-1-expressing human MDA-MB-231 breast cancer xenografts and in normal wild type mammary glands [5].

Methods

Animal models

All procedures involving the use of laboratory animals were approved by the Institutional Administrative Panel on Laboratory Animal Care at Stanford University. For induction of subcutaneous tumors, female homozygous nude mice (NU/J, The Jackson laboratory) were used and 2×10^6 cells of human strongly netrin-1-positive SKBR7 (N=9) or

weakly netrin-1-expressing MDA-MB-231 (N=9) breast cancer were subcutaneously inoculated in the hind limbs of mice at 4 weeks of age [5]. After 2 weeks, mice underwent USMI and *in vivo* immuno-localization of netrin-1. Female transgenic breast cancer-bearing (N=30) FVB/N-Tg(MMTV-PyMT)⁶³⁴Mul/J mice (MMTV-PyMT) and female, transgene-negative control littermates (N=15) were

used at 8 weeks of age for USMI and *in vivo* immuno-localization of netrin-1. At this point of disease progression, female MMTV-PyMT mice were bearing invasive mammary carcinoma [21,32,33]. For netrin-1 and Fc receptor blocking experiments, mice were injected 100 µg of NET1-H-mAb 24 h prior to imaging.

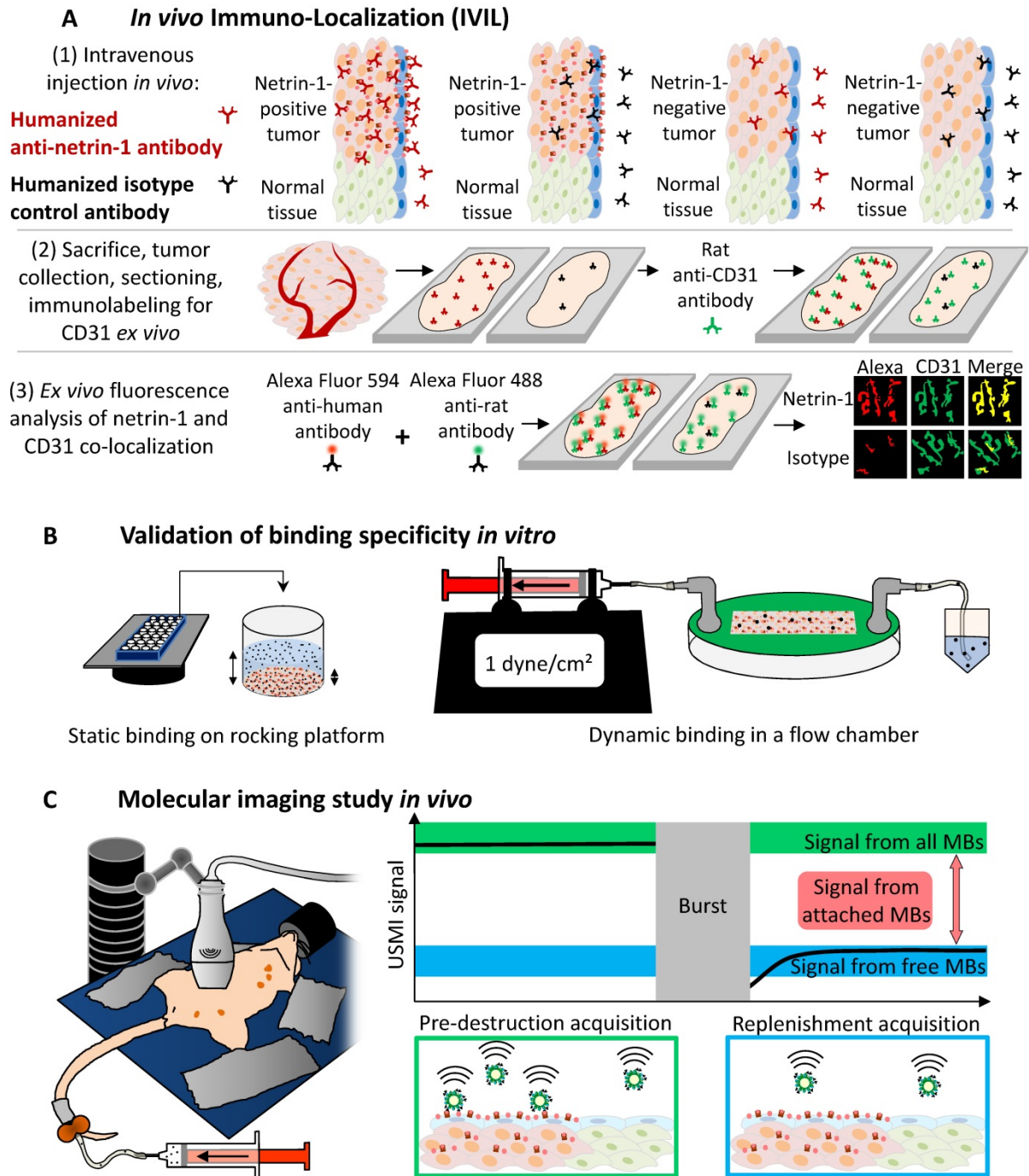


Figure 1. Study design. (A) *In vivo* immuno-localization (IVIL) analysis of endothelial expression of netrin-1. Netrin-1 was labeled *in vivo* and NET1-H-mAb and CD31 were revealed *ex vivo*. (B) Binding of targeted MBs to purified netrin-1 protein and netrin-1-overexpressing cells was evaluated under static conditions (by upright incubation in 24-well plates incubated on a rocking platform) or dynamic conditions (by inverted incubation with circulating MBs in a flow chamber). (C) Mouse models of human and murine breast cancer were used for *in vivo* imaging of netrin-1. Here, the MMTV-PyMT mouse lying on its back shows five mammary glands on each lateral side of the body. Anti-netrin-1-MBs were intravenously injected and imaged with an ultrasound imaging probe. Signal of bound MBs was quantified using the destruction-replenishment method.

In vivo immuno-localization (IVIL) staining of netrin-1 in endothelium

For netrin-1 immunostaining, a previously described IgG localization technique, here called IVIL, was applied, as standard *ex vivo* immunofluorescence staining was prevented by the specificity of NET1-H-mAb to native state netrin-1 as opposed to fixed netrin-1, which undergoes conformational changes and antigen masking during tissue fixation [32]. Targeted and control antibodies show passive accumulation in tumor tissues due to the enhanced permeability and retention effect and Fc-mediated molecular interactions [34–39]. To assess the degree of targeted accumulation, fluorescence signal from isotype control antibody and NET1-H-mAb were compared. After USMI with netrin-1-targeted and isotype control contrast agents and 24 h prior to tumor or normal mammary gland collection, living nude mice bearing subcutaneous human SKBR7 and MDA-MB-231 tumors, or living FVB/N-Tg(MMTV-PyMT)634Mul/J (MMTV-PyMT) mice bearing invasive mammary carcinoma and wild type mice with normal mammary glands were intravenously injected with either 100 µg of primary NET1-H-mAb or 100 µg of human IgG isotype control antibody (NBP1-97043, Novus Biologicals, Littleton, CO, USA). To remove freely circulating antibody, cardiac perfusion was performed with PBS, tumor tissues or mammary glands were isolated, flash frozen, and sectioned at 15 µm thickness on a cryostat. Endothelial cells were labeled with primary rat anti-mouse CD31 antibody (550274, BD Biosciences), followed by secondary Alexa 488-coupled goat anti-rat IgG (A11006, Life Technologies). No additional primary antibody targeted to netrin-1 was applied. NET1-H-mAb was revealed with Alexa Fluor 594-coupled goat anti-human IgG (A11014, Life Technologies). Stained sections of a maximum number of tumor samples and normal mammary glands were imaged on a LSM 510 confocal microscope (Zeiss) on the same day to allow relative quantification of fluorescence staining. Fluorescence images were analyzed with FIJI (Fiji Is Just ImageJ) software [40]. Endothelial presence of netrin-1 was indicated by co-registration of fluorescence signals for netrin-1 (Alexa Fluor 594) and CD31 (Alexa Fluor 488).

HeLa model cell lines

Generation of HeLa model cell lines either netrin-1-negative (HeLa-Ctrl) or netrin-1-positive (HeLa-Net1) were described previously [6]. The self-inactivating HIV-1-derived vector encoding netrin-1 under control of Human Elongation Factor-1 Alpha (EF-1 Alpha) promoter was inserted by

lentiviral transduction resulting in HeLa-Net1 cells. To create HeLa-Ctrl, a corresponding mock vector was used for lentiviral transduction.

Flow cytometry analysis of netrin-1 presentation on cell surfaces

Transduced netrin-1-positive (HeLa-Net1) and negative (HeLa-Ctrl) model cells and human umbilical vein endothelial cells (HUVEC) were used. Cell surface netrin-1 presentation was analyzed after heparin incubation, enzymatic digestion of heparan sulfate, and netrin-1 incubation via flow cytometry.

For the heparin competition experiment, cells were seeded at 4×10^6 cells/ 100 cm² flask. One day after seeding, the medium was removed and the flask was rinsed with PBS prior to addition of fresh medium complemented with 50 µg/mL of heparin (Heparin Sodium Salt, A3004, AppliChem). Twelve hours later, cells were collected by mechanical removal using a cell scraper.

For enzymatic digestion of heparan sulfate, cells were seeded at 1×10^6 cells/ 100 cm² flask. An enzyme cocktail composed of Heparinase III (H8891, Sigma), Heparinase I (H2519, Sigma) (both reconstituted in 20 mM Tris-HCl, pH 7.5, 0.1 mg/mL BSA, 4 mM CaCl₂, 150 mM NaCl buffer), Chondroitinase ABC (C2905, Sigma; reconstituted in 0.01% BSA in PBS), and β-Glucuronidase (G0251, Sigma; reconstituted in 0.1% BSA in PBS) was prepared. Cells were collected three days after seeding and were re-suspended in medium containing the enzyme cocktail for 1 h in the cell culture incubator with intermittent mixing. Treatment concentrations of the different enzymes were: Heparinase III, Heparinase I, and Chondroitinase ABC at 0.25 U/ 1×10^6 cells and β-Glucuronidase at 200 U/ 1×10^6 cells.

For incubation with exogenous netrin-1, HeLa-Ctrl were seeded at 1×10^6 cells/ 100 cm² flask and HeLa-Net1 at 2×10^6 cells/ 100 cm² flask. The netrin-1-containing supernatant of HeLa-Net1 and the control supernatant of HeLa-Ctrl were collected 3 days after seeding and sterile-filtrated. HeLa-Ctrl cells were collected 3 days after seeding, and then re-suspended in HeLa-Net1 supernatant or HeLa-Ctrl control supernatant for 1 h in the cell culture incubator with intermittent mixing.

For enzymatic digestion of heparan sulfate followed by incubation with exogenous netrin-1, HeLa-Ctrl cells were seeded at 1×10^6 cells/ 100 cm² flask. Cells were collected 3 days after seeding and re-suspended in medium containing the Heparinase III, Heparinase I, Chondroitinase ABC, and β-Glucuronidase enzyme cocktail for 1 h in the cell culture incubator with intermittent mixing. Next, the supernatant was removed by centrifugation and cells

were re-suspended in HeLa-Net1 supernatant for 1 h in the cell culture incubator with intermittent mixing.

Cells were labeled with NET1-H-mAb, with specificity for human and murine netrin-1, or humanized isotype control antibody (iso-mAb, Netris Pharma, Lyon, France) (2 μg antibody / 1×10^6 cells) [6]. For detection of heparan sulfate, mouse monoclonal anti-heparan sulfate (clone 10E4, Amsbio, Abingdon, UK) or the mouse monoclonal isotype control (clone MM-30, Abcam, Cambridge, UK) was used (1.5 μg antibody / 1×10^6 cells). Secondary PE-coupled anti-human IgG Fc (clone HP6017, BioLegend, San Diego, CA, USA) or Alexa Fluor 647-coupled anti-mouse IgG (A31571, Thermo Fisher, Waltham, MA, USA) was used (1 μg antibody / 1×10^6 cells). Cells were analyzed on a FACS Calibur (BD Biosciences, Franklin Lakes, NJ, USA). For analysis, debris and cell aggregates were excluded by gating on living single cells in FSCxSSC dot plots and 10,000 events were acquired. Fluorescence intensities were analyzed and fluorescence histograms were prepared with FSC Express 4 Flow Research Edition (De Novo Software, Glendale, CA, USA). Fluorescence signal ratios were calculated dividing marker intensities (in a.u.) by the respective isotype control intensity (in a.u.).

In vitro MB binding assays on purified netrin-1 protein and cell lines

To test the ability of netrin-1-targeted MBs to bind to recombinant netrin-1 protein, static and dynamic *in vitro* binding assays were performed as previously described [41,42].

MB binding to recombinant netrin-1 protein: To test the binding specificity of netrin-1-targeted MBs, a MB binding assay in 24-well plates under static binding conditions was performed as previously described [41]. Briefly, the wells of a 24-well plate were coated with different concentrations of netrin-1 protein (human recombinant, AdipoGen, San Diego, CA, USA). MBs were diluted to 1.2×10^8 MBs/mL in NaCl 0.9% + BSA 1% in H_2O and 350 μL of MB suspension was used per well. The plate was incubated in upright position on a rocking platform (25 rpm, 5 min) at room temperature so that MBs contacted with the coated well surface by liquid turbulences. Before microscopy (Zeiss Axiovert, Metamorph, Marly le Roi, France), unbound MBs were removed by incubation on a plate shaker (3x, 300 rpm, 10 s). MBs bound to netrin-1 were automatically counted by analyzing photomicrographs with MATLAB 2013 (The MathWorks, Natick, MA, USA) (see Supplementary Material).

Effect of buffer on MB binding: To test the effect of buffer on MB binding, a 96-well plate binding

assay in inverted position was performed as previously described [41]. Briefly, a 96-well plate was coated at 4 $\mu\text{g}/\text{mL}$ of netrin-1. MBs were diluted to 1.2×10^7 MBs/mL either in 1% BSA, 0.9% NaCl in H_2O or in 50% human plasma, 0.09% NaCl in H_2O . MBs were incubated in 96-well plates (350 μL of MB suspension per well) in upside-down position at 4 $^\circ\text{C}$ so that MBs got in contact with the coated well surface by buoyancy. Plates were returned to the right-side up position and photomicrographs were recorded with an inverted microscope (Nikon Eclipse Ti-S, Champigny sur Marne, France). This procedure allowed unbound MBs to float above the focal plane, eliminating the need for a separate washing step.

Effect of temperature on MB binding: To verify the effect of temperature on MB binding, MBs were diluted to 1.2×10^7 MBs/mL in 100% plasma (human Na-Heparin, DivBioScience, Ulvenhout, The Netherlands) and incubated in a netrin-1-coated (4 $\mu\text{g}/\text{mL}$) 96-well plates in upside-down position either at room temperature or at 37 $^\circ\text{C}$ for 30 min. Plates were returned to the right-side up position and photomicrographs were recorded with an inverted microscope (Nikon Eclipse Ti-S).

Effect of shear stress on MB binding: To study the effect of shear stress on MB binding, a parallel plate flow chamber (gasket B, Glyco Tech, Maryland, USA) was used in combination with a 35 mm-Corning dish that was previously coated with netrin-1 at 4 $\mu\text{g}/\text{mL}$. To seal the chamber a vacuum pump was used (BioBlock, Fisher Scientific, Illkirch, France). The flow chamber had a flow path of 2.5 cm width, 0.254 mm height, and 10 mm length. MBs were diluted to 5×10^6 MBs/mL in 1% BSA, 0.9% NaCl in H_2O . Using a syringe pump (PHD ULTRA, Harvard Apparatus, Les Ulis, France), physiological shear stresses of 1 or 2 dynes/cm², which are equivalent to flow rates of 212 and 424 μL , were created to simulate shear stresses of tumor blood vessels according to previously described protocols [16,23,42]. MBs circulated for 5.5 min in the flow chamber. MB circulation and attachment were recorded via time-lapse video-microscopy (Leitz Laborlux S, Zeiss AxioCam 105 color). Attached MBs in video sequences were automatically counted using MATLAB 2013 (The MathWorks) (see Supplementary Material).

MB binding on HeLa-Ctrl and HeLa-Net1 cells: To verify binding of anti-netrin-1 MBs to HeLa-Ctrl and HeLa-Net1 cells, a binding assay in 96-well plate format in inverted position was performed. Cells were seeded at 1×10^4 cells per well. Three days after seeding, functionalized MBs (diluted to 1.2×10^7 MBs/mL in 50% human plasma, 0.9% NaCl in H_2O) were added to the 96-well plate (350 $\mu\text{L}/\text{well}$) and incubated in upside-down position at 4 $^\circ\text{C}$ for 30 min.

Plates were returned to the right-side-up position and photomicrographs were recorded with an inverted microscope (Nikon Eclipse Ti-S).

MB binding on breast cancer cells: In the study of MB binding to breast cancer cells, the following cell lines were included: human SKBR7 and MDA-MB-231 (kindly provided by P. Mehlen, CRCL, Inserm U1052, Lyon, France). MB binding experiments on breast cancer cell lines were performed under dynamic conditions in flow chambers. Cells were seeded at 4.5×10^5 cells in 35-mm Corning dishes. Two days after seeding, MBs were diluted to 5×10^6 MBs/mL and circulated for 12 min in the parallel plate flow chamber at a shear stress of 1 dyne/cm². Flow chamber assays under the illuminating microscope were performed at a temperature of 25 to 26 °C as monitored by infrared thermometry. Circulating and attached MBs were recorded by time-lapse videomicroscopy and the image sequences were automatically analyzed. Cellular vesicles and MBs were distinguished based on the image analysis depicting cells prior and subsequent to incubation with MBs.

In vivo imaging of netrin-1

Imaging protocol: Tumors of MMTV-PyMT mice were imaged when they reached approximately 5 mm in diameter. These were compared with age-matched wild type mice with mammary glands of approximately 4 mm in diameter. MMTV-PyMT and wild type mice were depilated using a depilation cream (Nair™ Lotion With Aloe & Lanolin", Church & Dwight Co., Inc., Ewing, NJ, USA). SKBR7 tumors were imaged when they reached approximately 10 mm in diameter and MDA-MB-231 tumors when they reached approximately 8 mm in diameter. Nude mice lacking hair did not require depilation prior to imaging. During imaging, mice were under anesthesia at 2% isoflurane in oxygen at 2 L/min and kept warm using a heated stage and a heat lamp. For coupling of the ultrasound transducer, pre-warmed gel was applied on the skin of the regions to be imaged. The small-animal high resolution imaging system Vevo 2100 (VisualSonics, Toronto, CA) in combination with the MS-250 transducer (center frequency at 21 MHz, lateral resolution of 165 μm and axial resolution of 75 μm, focal length at 8 mm) that was immobilized on an adjustable stand was used for all acquisitions. Scanning through the tumor tissue in ultrasound B-mode, the 2D cross-section showing the tumor or gland at its biggest diameter was identified and selected for image acquisition. Shortly before imaging, MBs were functionalized with biotinylated NET1-H-mAb (MB_{Netrin-1}) or biotinylated human IgG isotype control antibody (MB_{isotype}) (NBP-1-96855,

Novus Biologicals, Littleton, CO, USA) (50 μg antibody/ 1.6×10^9 MBs in one vial). The same batch of MBs was used for all *in vivo* imaging studies. A 27 G needle was used for bolus injection of a total of 1×10^8 MBs in 100 μL of PBS via a catheter (orange butterfly) into the tail vein. The catheter was flushed post injection with 50 μL of PBS to ensure the total MB dose was administered. Tumors or normal mammary glands were imaged 4-10 min post intravenous bolus injection of MBs according to previously described protocols [21,24,43]. To image several different tumors in the same mouse after a single MB injection, the transducer was moved from the first tumor to the next and a novel destruction-replenishment acquisition was performed. USMI was performed in contrast mode with an emission frequency of 21 MHz and a reception frequency range of 13-24 MHz, transmit power of 10%, mechanical index at 0.2, and dynamic range of 40 dB. The destruction-replenishment method was used for quantification of the targeted enhancement between pre-burst signal from free-circulating and bound MBs, and replenishment signal from only free-circulating MBs acquired immediately after a destructive pulse (**Figure 1C**) as previously described [21]. Between acquisitions with different types of MBs in the same mouse, a lag time of a minimum of 25 min was included for MB wash-out, which was verified by CEUS [44]. The order of injections with different MB types was randomized. B-mode was used for anatomical guidance to image the same position before and after blocking with NET1-H-mAb. USMI acquisitions with MB_{Netrin-1} and MB_{isotype} prior to blocking were performed on day 1 of the imaging protocol. USMI acquisitions post blocking were performed on day 2; i.e. 24 h post injection of NET1-H-mAb for blocking.

Imaging data analysis: The imaging sequence was composed of 166 pre-burst frames (=12 s), a burst, and 130 replenishment frames (=10 s). To burst the MBs, a continuous high-power destructive pulse of 3.7 MPa (100% transmit power, mechanical index of 0.63, duration of 1 s) was applied. The pre-burst and replenishment frames were used to determine bound MB signal: short sequences between two respirations were manually selected; the pre-burst frame was selected right before applying the burst and the post-burst frame was selected a few seconds after burst when the circulating MBs reached the imaging frame, which was indicated by signal saturation. To avoid over- or underestimation of imaging signal in absolute values due to inter-tissue heterogeneity, the molecular imaging signals were calculated as the targeted enhancement ratio (T.E. (r)) in linear units (l.a.u.) using the VevoLab software:

$$\text{T.E. (r)} = (\text{pre-burst signal in I.a.u.}) / (\text{post-burst signal in I.a.u.}).$$

To avoid the presentation of data with artificially high background signal, the imaging data was then converted into percentages according to the following formula:

$$\text{Molecular imaging signal in \%} = (1 - (1 / \text{T.E. (r)})) \times 100\%.$$

For visual presentation, image panels were provided that present tumors on anatomical B-mode images in grey (upper row in figure panels) and the respective contrast-enhanced ultrasound image in brown (lower row in figure panels) including the color-coded USMI signal. These images were exported from VevoCQ software, which allows visualization of the USMI signal distribution in the region of interest (green contour) as the differential targeted enhancement (d.T.E. in I.a.u.):

$$\text{d.T.E.} = (\text{pre-burst signal}) - (\text{post-burst signal}).$$

For comparison of molecular imaging signal between different tumor models, the differential USMI signal was calculated by subtracting the background signal (quantified with $\text{MB}_{\text{isotype}}$) from the targeted molecular imaging signal (quantified with $\text{MB}_{\text{Netrin-1}}$): $\Delta(\text{MB}_{\text{Netrin-1}} - \text{MB}_{\text{isotype}})$ USMI signal (%). This was calculated for every tumor. Then, the individual tumor values were used to calculate the mean $\Delta(\text{MB}_{\text{Netrin-1}} - \text{MB}_{\text{isotype}})$ USMI signal and SEM for each tumor model, and the statistical analysis was performed.

Netrin-1 expression analysis by q-RT-PCR

Total RNA was extracted from biopsies using the TRIzol-Reagent (Ambion, Life Technologies) and 1 μg was reverse-transcribed using the iScript cDNA Synthesis kit (BioRad). Real-time quantitative RT-PCR was performed with a LightCycler 2.0 apparatus (Roche) using LightCycler® TaqMan® Master kit (Roche, Basel, Switzerland). Reaction conditions for all optimal amplifications, as well as primers selection were determined as already described [6]. The ubiquitously expressed human or murine hypoxanthine phosphoribosyl transferase (HPRT) gene was used as an internal loading control. The following primers were used: murine netrin-1 forward - 5'-GCAAGCTGAAGATGAACATGA-3', reverse - 5'-CTTTGTCGGCCTTCAGGAT-3'; murine HPRT forward - 5'-TCCTCCTCAGACCGCTTTT-3', reverse - 5'-CCTGGTTCATCATCGCTAATC-3'; human netrin-1 forward - 5'-AAAAGTACTGCAAG AAGGACTATGC-3', reverse - 5'-CCCTGCTTATAC ACGGAGATG-3'; human HPRT forward - 5'-TGACCTTGATTTATTTTGCATACC-3', reverse -

5'-CGAGCAAGACGTTTCAGTCCT-3'.

Statistical analysis

The number of samples or replicates per experimental condition or group is indicated as N. Standard errors (STD) or standard errors of the mean (SEM) are shown in graphs as indicated in the figure legends. Differences between two groups were tested by Student's *t*-test. Comparisons of more than two groups were performed using ANOVA followed by a Tukey-Kramer post-hoc test. Statistical *p*-values are indicated in the graphs. The absence of statistically significant *p*-values indicated that differences were not significant. Statistical analyses are specifically indicated in every figure legend. Details about the receiver operating characteristic (ROC) curve are described in Supplementary Material.

Results

In vivo immuno-localization of netrin-1

First, we assessed whether netrin-1 was localized on vascular endothelial cells of netrin-1-positive tumors and was an accessible molecular target for USMI. IVIL and immunofluorescence showed that the anti-netrin-1 antibody signal was present in epithelial and endothelial layers of human SKBR7 tumors (**Figure 2**). Comparison of fluorescence intensities of NET1-H-mAb and isotype control that were co-localized with CD31 showed a significantly greater extent of immunofluorescence with NET1-H-mAb in netrin-1-positive SKBR7 (NET1-H-mAb: fluorescence intensity of 51.54 ± 4.2 a.u.; isotype control: 38.6 ± 3.4 a.u.; $p=0.035$), while there was no difference between NET1-H-mAb and isotype control in weakly netrin-1-expressing human MDA-MB-231 (NET1-H-mAb: fluorescence intensity of 28.29 ± 2.5 a.u.; isotype control: 34.17 ± 4.3 a.u.; n.s.) (**Figure 2**). Q-PCR confirmed netrin-1 expression in SKBR7 tumor tissues while netrin-1 was barely detectable in MDA-MB-231 tumors (**Figure S1**). Thus, SKBR7 breast tumors with epithelial netrin-1 expression showed NET1-H-mAb staining in the tumor endothelium, suggesting an association between netrin-1 expression in tumor cells and endothelial presentation of netrin-1.

Netrin-1 on cell surfaces

Flow cytometry analysis confirmed netrin-1 presentation on the cell surface of HeLa-Net1 model cells while netrin-1 was not detected by Western blot and flow cytometry analysis of HeLa-Ctrl cells (**Table 1**, **Figure S2** and **Figure S3A**). Incubation of HeLa-Net1 cells with heparin reduced netrin-1 presentation by 69.5% (**Table 1** and **Figure S3B**). The use of an enzyme cocktail degrading heparan sulfates

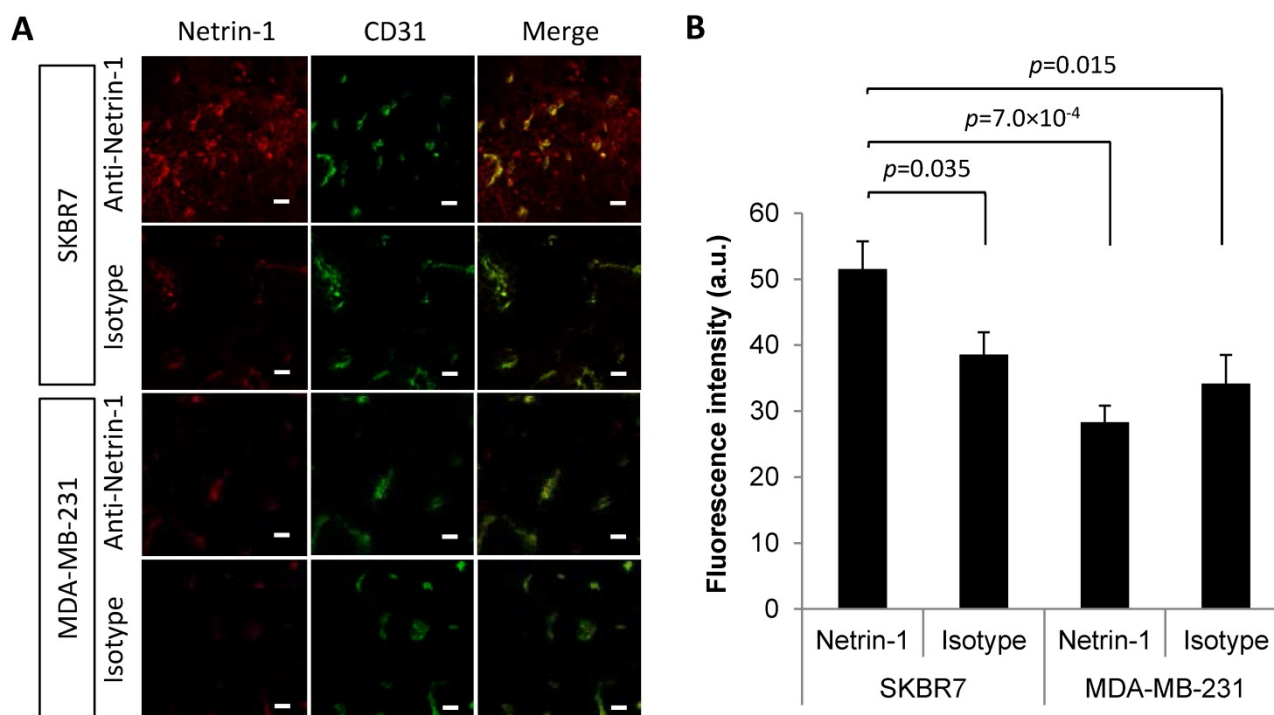


Figure 2. *In vivo* immunolocalization (IVIL) analysis of netrin-1 expression in subcutaneous human SKBR7 and MDA-MB-231 breast cancer. (A) Representative IVIL images for netrin-1, CD31, and their co-localization (merge). (B) Quantification of IVIL fluorescence intensity of netrin-1 that is co-localized with CD31 indicates significantly enhanced netrin-1 signal in endothelial cells of SKBR7 breast tumors. All groups were compared to netrin-1 fluorescence intensity in SKBR7 tumors using Student's *t*-test. Scale bars indicate 20 μ m. N=6 tumors (of three mice) per group; error bars present SEM.

resulted in depletion of heparan sulfate by 95.4% and netrin-1 by 55.9% in HeLa-Net1 cells (Table 1 and Figure S3C). Incubation of HeLa-Ctrl cells with exogenous netrin-1 resulted in strong presentation shown by a 49-fold rise in signal intensity (Table 1 and Figure S3D). The enzymatic digestion of heparan sulfate and netrin-1 addition to HeLa-Ctrl cells induced a decrease of heparan sulfate by 76.2%, and of netrin-1 by 37.4% (Table 1 and Figure S3D). HeLa-Net1 cells revealed a lower heparan sulfate level than HeLa-Ctrl cells (50.9% of HeLa-Ctrl), but the heparan sulfate signal of HeLa-Ctrl cells dropped once netrin-1 was added (Table 1 and Figure S3C-D). HUVEC endothelial cells did not naturally present netrin-1, but addition of exogenous netrin-1 resulted in presentation with a 2.5-fold higher signal compared with untreated HUVEC cells (Table 1 and Figure S3E). On HUVEC cells, heparin incubation again prevented netrin-1 presentation (Table 1). To summarize, netrin-1 was detected on cell surfaces of cancer and endothelial cells using the anti-netrin-1 antibody and netrin-1 presentation was at least partially mediated by heparan sulfate proteoglycans.

Table 1. Netrin-1 interaction on cell surfaces studied in HeLa-Ctrl and HeLa-Net1 model cells, and HUVEC endothelial cells studied by flow cytometry. Mean fluorescence intensities were converted into signal ratios by division of marker intensity by the respective isotype control. Cell surface presentation of netrin-1, the effect of heparin addition (12 h), enzymatic digestion of cell surface glycans (3 d), addition of exogenous netrin-1 (1 h), a combination of enzymatic digestion of glycans and subsequent netrin-1 addition, and a combination of heparin pre-treatment and addition of exogenous netrin-1 were tested. For enzymatic treatment, a cocktail containing Heparinase I, Heparinase III, Chondroitinase ABC and Glucuronidase was used. Netrin-1 was produced by HeLa-Net1 cells. N=1.

Netrin-1-positive and -negative model cell lines				
Cell line	Marker	Signal ratio		
		Untreated		
HeLa-Ctrl	Netrin-1	0.9		
HeLa-Net1	Netrin-1	2.6		
Heparin				
Cell line	Marker	Signal ratio		
		Untreated	Heparin	
HeLa-Net1	Netrin-1	8.2	2.5	
	Heparan sulfate	135.8	97.2	
Enzymatic degradation of cell surface glycans				
Cell line	Marker	Signal ratio		
		Untreated	Enzymes	
HeLa-Net1	Netrin-1	11.8	5.2	
	Heparan sulfate	28.1	1.3	
Addition of Netrin-1 and enzymatic digestion of cell surface glycans				
Cell line	Marker	Signal ratio		
		Untreated	Netrin-1	Enzymes + Netrin-1
HeLa-Ctrl	Netrin-1	0.9	44.1	27.6
	Heparan sulfate	55.2	34.8	8.3
Netrin-1 presentation on HUVEC endothelial cells				
Cell line	Marker	Signal ratio		
		Untreated	Netrin-1	Heparin & Netrin-1
HUVEC	Netrin-1	1.1	2.7	1.4

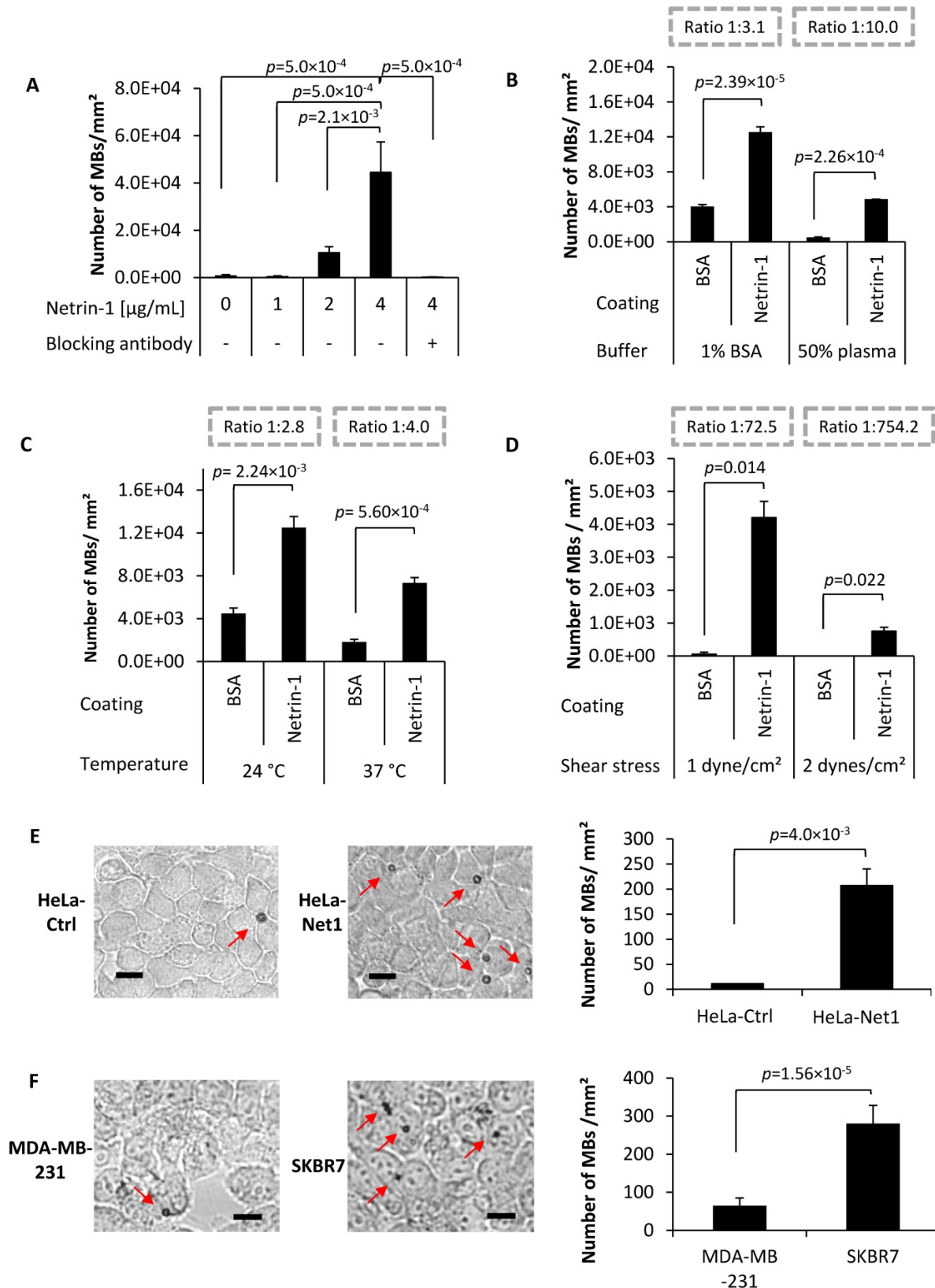


Figure 3. MB binding in vitro on purified netrin-1 protein and on netrin-1-overexpressing cells. (A) Anti-netrin-1-MBs binding specificity showed significant differences between MB concentration at 4 $\mu\text{g/mL}$ and all other conditions (one-way ANOVA ($F(5,12) = 12.55, p=0.0002$) followed by Tukey-Kramer post-hoc test). $N=3$. **(B)** Anti-netrin-1-MB binding in presence of human plasma. Binding ratios (numbers of MBs binding to BSA vs. number of MBs binding to netrin-1 protein) are depicted in dashed grey boxes. $N=3$. **(C)** Anti-netrin-1-MB binding at body temperature. $N=3$. **(D)** Anti-netrin-1-MB binding under shear stress. $N=3$. **(E)** Anti-netrin-1-MB binding on HeLa-Ctrl and HeLa-Net1 cells under static conditions in presence of plasma. $N=3$. **(F)** Anti-netrin-1-MB binding on human strongly netrin-1-expressing SKBR7 and weakly netrin-1-expressing MDA-MB-231 breast cancer cells under shear stress (1 dyne/ cm^2). $N=2$. Except for (A), two-group comparisons were performed with Student's t-test. Error bars present SEM; scale bars indicate 10 μm .

Preparation of netrin-1-targeted MBs and validation of MB binding *in vitro*

Next, a netrin-1-targeted UCA was created for USMI (Figure S4 and Figure S5A-D) and validated in *in vitro* binding assays. Netrin-1-targeted MBs bound to netrin-1 in a dose-dependent manner (Figure 3A). Netrin-1 blocking with NET1-H-mAb prior to incubation with anti-netrin-1-MBs significantly reduced binding (Figure 3A). The use of plasma buffer and a rise in temperature to 37 °C improved the ratio of MB binding to BSA vs. binding to netrin-1 protein (Figure 3B-C). Under dynamic conditions in flow chamber assays, MBs bound to netrin-1 at a shear stress of 2 dynes/cm² and essentially did not bind to BSA (Figure 3D). MB binding was significantly higher on HeLa-Net1 cells than on HeLa-Ctrl cells in static binding assays (Figure 3E). In agreement with q-RT-PCR analysis of netrin-1 expression (Figure S6), MB binding in flow chamber assays was significantly higher on netrin-1-positive human SKBR7 cells than on barely netrin-1-expressing human MDA-MB-231 cells (Figure 3F) [5]. In short, the UCA was able to bind to recombinant netrin-1 and to tumor cells expressing high levels of netrin-1.

In vivo imaging of netrin-1 in subcutaneously engrafted breast tumors of human and murine origin

To validate the use of MBs *in vivo*, breast tumors were imaged with NET1-H-mAb-functionalized MBs (MB_{Netrin-1}) and human isotype control MBs (MB_{Isotype}). Netrin-1-positive human SKBR7 breast tumors showed a significantly higher molecular imaging signal with MB_{Netrin-1} compared with MB_{Isotype} (28.2% ± 4.3% signal intensity vs. 13.7% ± 1.8% signal intensity; $p=4.64 \times 10^{-3}$) (Figure 4A). After blocking of netrin-1 with NET1-H-mAb, the signal of MB_{Netrin-1} dropped to that of MB_{Isotype}, suggesting binding of MB_{Netrin-1} to netrin-1. To assess antibody Fc-mediated signal, MB_{Isotype} signal intensity was detected before and after injection of NET1-H-mAb, but no change in signal was observed. There was no significant difference between MB_{Netrin-1} (25.5% ± 4.6% signal intensity) and MB_{Isotype} (19.8% ± 3.9% signal intensity) in human MDA-MB-231 breast tumors with netrin-1 expression levels below the limit of detection of flow cytometry and Western blot analysis (Figure 4B). Taken together, MB_{Netrin-1} bound in SKBR7 tumors, but not in MDA-MB-231. MB_{Isotype} showed higher signal in MDA-MB-231 than in SKBR7 tumors, hence indicating heterogeneous signals with the same UCA in different tumor tissues, although the differences were not significant (Figure 4A-B). Molecular imaging signal in % was derived from d.T.E. (r) values provided by the VevoLab software. Both approaches

(molecular imaging signal in % and d.T.E. in l.a.u.) indicated significantly enhanced signal with netrin-1-targeted MBs in SKBR7 tumors, validating the improved calculation method converting molecular imaging signal into % and eliminating artificially high background signal (Figure S7 vs. Figure 4 and Figure 5). The calculation of the differential molecular imaging signal in %, which excluded background signal as detected with MB_{Isotype} from the analysis, showed that SKBR7 tumors had 4.7-times higher molecular imaging signal than MDA-MB-231 tumors (17.8% ± 3.4% vs. 3.8% ± 4.8% signal intensity; $p=0.044$) (Figure 4C). In short, *in vivo* imaging of netrin-1 proved feasible in human subcutaneous tumor models and reflected netrin-1 overexpression in SKBR7 tumors.

In vivo imaging of netrin-1 in a transgenic mouse model of breast cancer

Next, USMI was performed in a transgenic murine breast cancer model (MMTV-PyMT) that recapitulates spontaneous breast tumor development, but whose netrin-1 expression status was unknown until now. Breast tumors of MMTV-PyMT mice were compared with healthy mammary glands of wild-type mice. In MMTV-PyMT breast tumors, MB_{Netrin-1} resulted in 44.8% ± 2.2% signal, which was significantly different from MB_{Isotype} with 32.0% ± 2.9% ($p=8.18 \times 10^{-4}$) (Figure 5A). After blocking with NET1-H-mAb, MB_{Netrin-1} and MB_{Isotype} showed similar intensities: MB_{Netrin-1} at 33.7% ± 3.4% and MB_{Isotype} at 26.4% ± 3.3%. In normal glands, there was no significant difference between signals of both MB types (Figure 5B). USMI signal detected with MB_{Isotype} in breast tumors was significantly higher than the signal observed in normal mammary glands (32.0% ± 2.9% for breast cancer vs. 9.0% ± 2.2% for normal glands; $p=2.72 \times 10^{-8}$) indicating heterogeneity in unspecific background signal (Figure 5A-B). The differential USMI signal, which normalizes the molecular imaging signal to the non-specific background signal, showed a 2.7-fold higher imaging signal in MMTV-PyMT tumors compared with normal mammary glands (14.7% ± 2.0% vs. 5.5% ± 1.2% signal intensity; $p=0.0003$) suggesting that MMTV-PyMT tumors were netrin-1-positive (Figure 5C).

Q-RT-PCR confirmed netrin-1 overexpression in MMTV-PyMT breast tumors (26.8 ± 16.6-fold expression relative to HPRT in tumors in contrast to a 1.8 ± 0.4-fold expression in normal breast glands; $p=0.024$) (Figure 6A). IVIL and immunofluorescence analysis showed specific labeling of the CD31-positive MMTV-PyMT breast tumor endothelium with anti-netrin-1 antibody compared to isotype control

antibody (fluorescence intensity of 50.3 ± 3.5 a.u. vs. 37.6 ± 1.8 a.u.; $p=4.8 \times 10^{-3}$) (Figure 6B). In normal breast glands, NET1-H-mAb and isotype control antibody showed no significant differences in fluorescence intensity (39.7 ± 3.5 a.u. vs. 41.3 ± 4.8 a.u., respectively) (Figure 6B). Endothelial localization of netrin-1 in all netrin-1-positive tumor models was

further confirmed by co-localization with CD146, an endothelial receptor with affinity for netrin-1 (Figure S8) [11]. Taken together, *in vivo* imaging results for MMTV-PyMT and wild type mice were confirmed by *ex vivo* analysis of netrin-1 presentation.

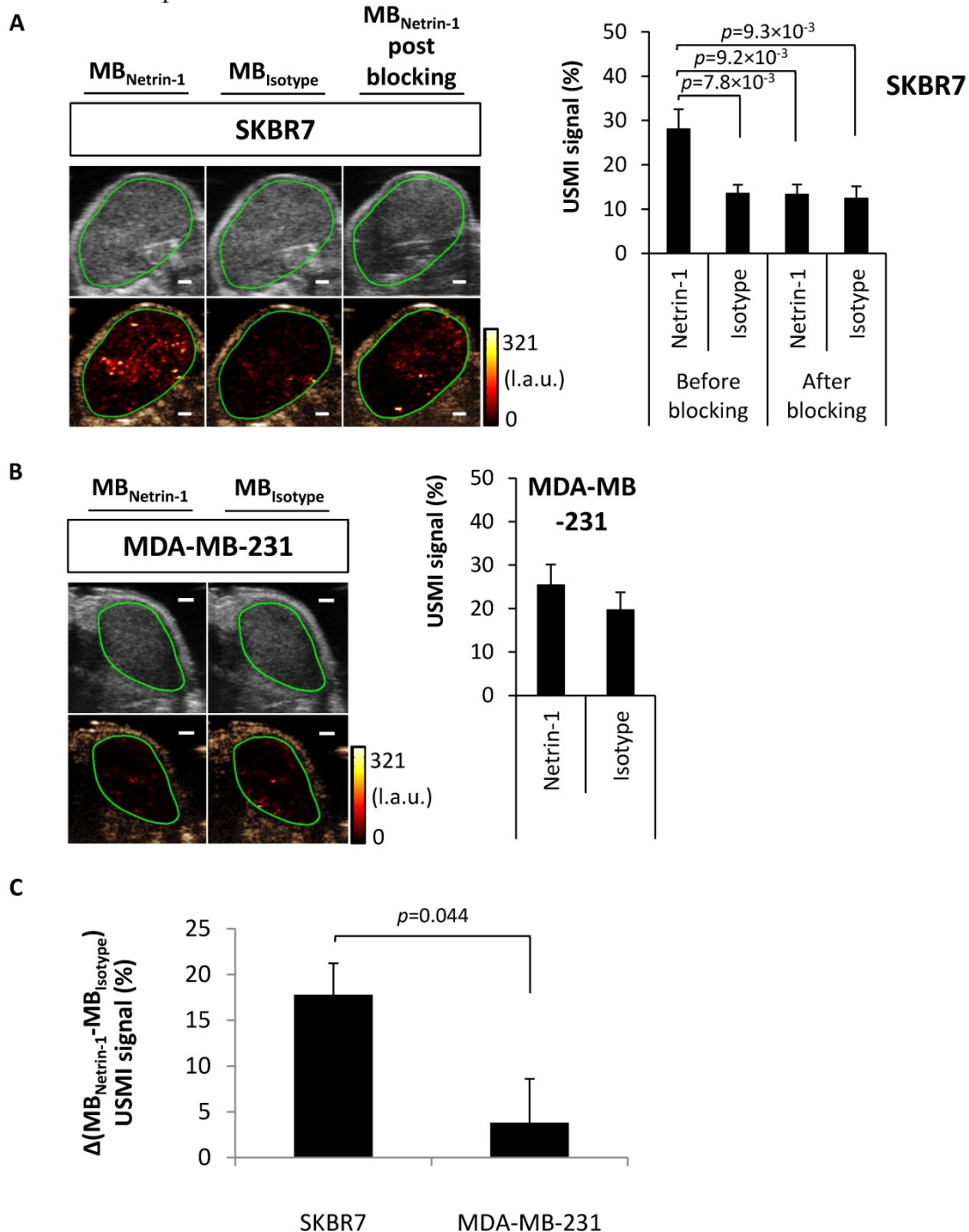


Figure 4. Assessment of USMI for netrin-1 detection using anti-netrin-1-MBs (MB_{Netrin-1}) and isotype control MBs (MB_{Isotype}). (A) Netrin-1-positive human subcutaneous SKBR7 breast tumors in nude mice were imaged with both MB types prior to and post blocking with NET1-H-mAb (N=9). (B) Weakly netrin-1-expressing human subcutaneous MDA-MB-231 breast tumors were imaged with both MB types (N=9). Image panels present ultrasound B-mode images in grey (upper row) and the respective contrast-enhanced ultrasound image in brown (lower row) including the color-coded USMI signal distribution in the region of interest (green contour). Scale bars indicate 1 mm; error bars indicate SEM. (C) For comparison of molecular imaging signal between SKBR7 tumors and MDA-MB-231 tumors, the differential USMI signal was calculated by subtracting the background signal (quantified with MB_{Isotype}) from the targeted molecular imaging signal (quantified with MB_{Netrin-1}): $\Delta(\text{MB}_{\text{Netrin-1}} - \text{MB}_{\text{Isotype}})$ USMI signal (%). Results show a significantly enhanced signal in SKBR7 tumors compared to MDA-MB-231 tumors. SKBR7 (N=9), MDA-MB-231 (N=9); Error bars indicate SEM. In all figures, two-group comparisons were performed with Student's t-test.

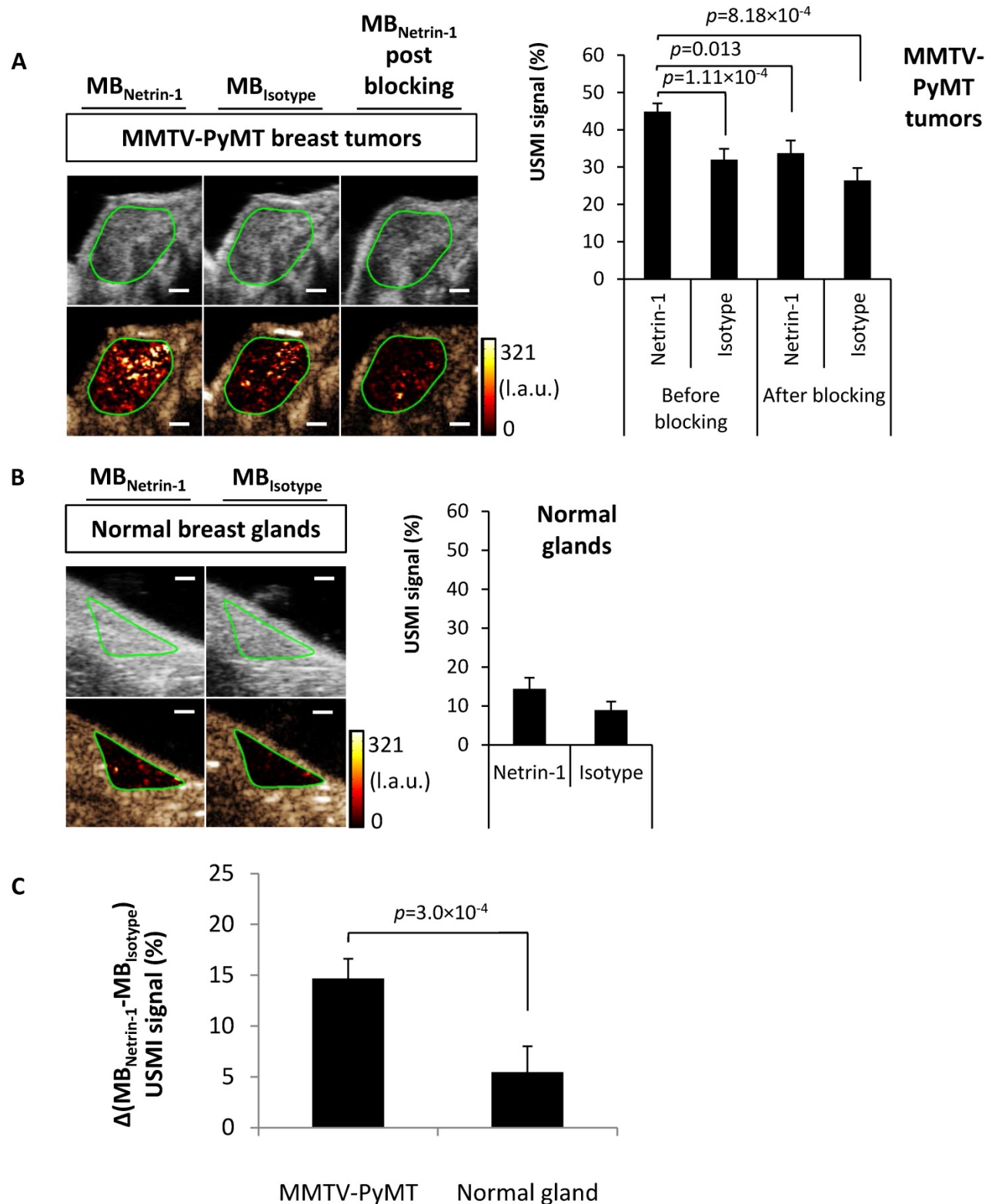


Figure 5. Feasibility of USMI of netrin-1 in the murine transgenic MMTV-PyMT breast cancer model. (A) USMI signal intensities obtained with anti-netrin-1-MBs (MB_{Netrin-1}) and isotype control MBs (MB_{Isotype}) prior to and post blocking of netrin-1 with NET1-H-mAb in MMTV breast cancer (N=30). **(B)** As a control, normal mammary glands of wild type mice were imaged with both types of MBs (N=15). Image panel presents ultrasound B-mode images in grey (upper row) and the respective contrast-enhanced ultrasound image in brown (lower row) including the color-coded USMI dTE signal distribution ((pre-burst) – (post-burst)) in the region of interest (green contour). Scale bars indicate 1 mm; error bars indicate SEM. **(C)** For comparison of molecular imaging signal between transgenic murine tumors and normal mammary glands, the differential USMI signal ($\Delta(\text{MB}_{\text{Netrin-1}} - \text{MB}_{\text{Isotype}})$ USMI signal (%)) was calculated and showed a significantly enhanced signal in MMTV-PyMT tumors compared to normal glands. MMTV-PyMT breast cancer (N=30), normal mammary glands (N=15); error bars indicate SEM. In all figures, two-group comparisons were performed with Student’s t-test.

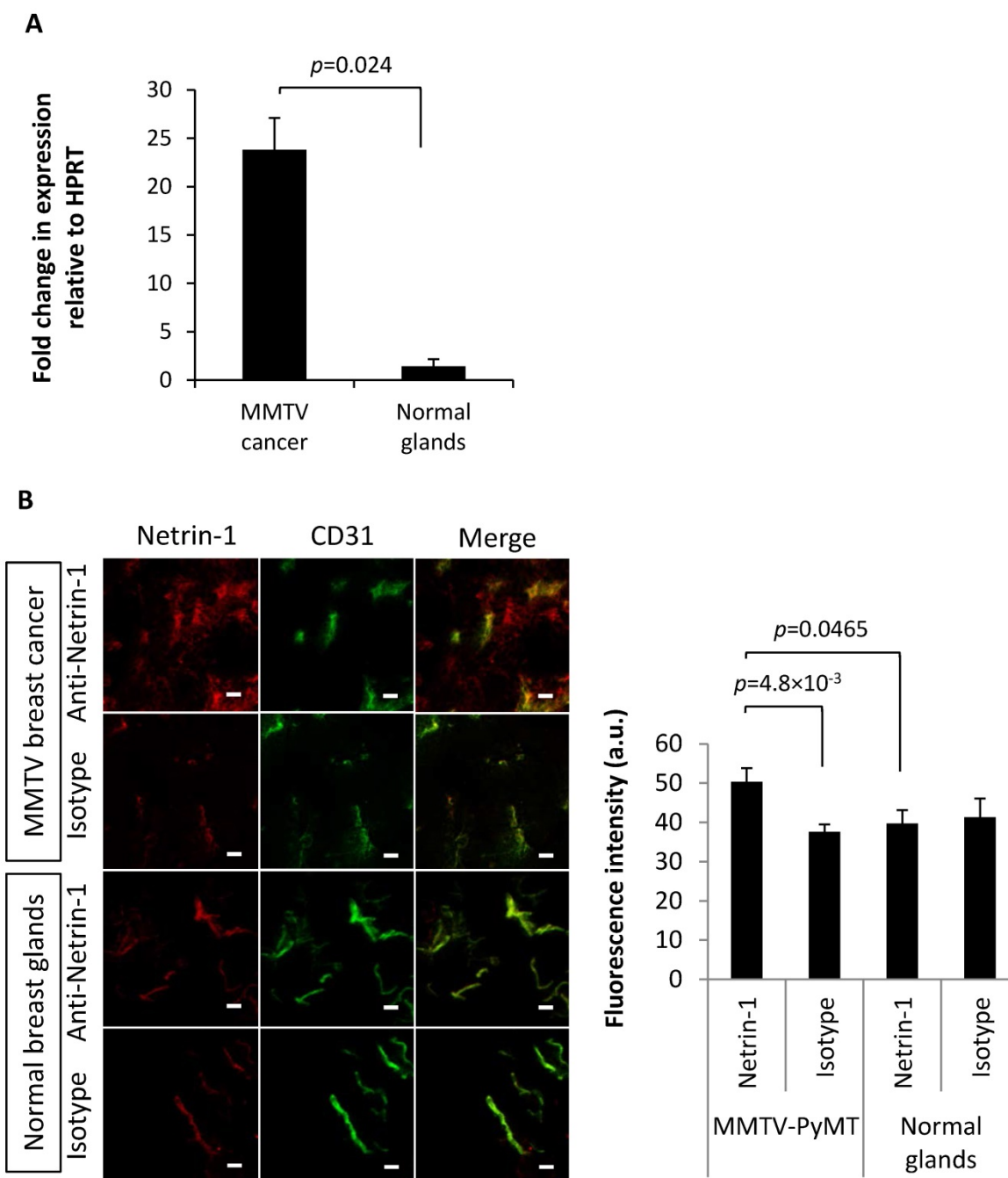


Figure 6. Ex vivo analysis of netrin-1 expression in the MMTV-PyMT breast cancer model. Q-RT-PCR analyses (A) and *in vivo* immuno-localization (IVIL) (B) of netrin-1 expression confirm the strong expression of netrin-1 in MMTV-PyMT tumors and significantly weaker expression of netrin-1 in normal mammary glands. N=13 tumors (of two mice) per group of MMTV-PyMT and N=7 mammary glands (of one mouse) per group of normal glands in IVIL; N=4 for q-RT-PCR; error bars present SEM; IVIL scale bars indicate 20 μ m. In all figures, two-group comparisons were performed with Student's *t*-test.

Finally, a receiver operating characteristic (ROC) curve was estimated based on the MMTV-PyMT tumor vs. normal gland USMI signal in % derived from netrin-1-targeted MBs only (and not from the difference between netrin-1-targeted and isotype control MBs). The datasets contained 45 imaging samples thus enabling a statistically robust estimation of the curve. The area under the curve (AUC) and confidence interval (CI) showed that USMI based on MB_{Netrin-1} signal alone allowed differentiating between

normal mammary glands and MMTV-PyMT breast tumors (AUC: 0.98; 95% CI: 0.95-1) with high diagnostic accuracy (Figure S9). At a threshold level as low as 33.3%, normal mammary glands of wild type mice and breast tumors in MMTV-PyMT mice were predicted to be diagnosed with a sensitivity of 90% (95% CI: 80-100) and a specificity of 100% (95% CI: 98-100). These observations confirm the potential diagnostic value of USMI for the detection of netrin-1 in tumors.

Discussion

In vivo immuno-localization of netrin-1

Netrin-1 expression by endothelial model cells remains controversial [8,45]. To understand whether netrin-1 is presented on the endothelium of netrin-1-overexpressing tumors, we applied IVIL and showed netrin-1 expression in the tumor epithelium and co-localization with endothelial CD31 and CD146 in human SKBR7 breast tumors. However, the results did not allow conclusions on the origin of netrin-1 – whether it was secreted by epithelial tumor cells and diffused to the endothelium or whether the tumor induced netrin-1 expression in the endothelium. Alternatively, a third explanation for co-localization of netrin-1 and CD31 could be a structurally impaired endothelial lining interspersed with netrin-1-overexpressing tumor cells [46].

Netrin-1 on cell surfaces

Netrin-1 is a secreted ligand containing a heparin-binding domain, and heparan sulfate proteoglycans act as flow sensors on the luminal side of endothelial cells [1,47]. Thus, heparan sulfate proteoglycan-mediated netrin-1 presentation on cell surfaces was studied. The data confirmed removal of netrin-1 from the cell surface after heparin addition or depletion of heparan sulfate proteoglycans. Further studies are required to understand whether other netrin-1-binding molecules mediate netrin-1 presentation on cell surfaces [45]. The incubation of cells with netrin-1 protein showed that netrin-1 binding to the cell surface was independent of the origin of netrin-1, i.e., whether it was an autocrine or exocrine production. Netrin-1 binding on cell surfaces interfered with the detection of heparan sulfate, suggesting direct or indirect netrin-1 binding to the anti-heparan sulfate antibody epitope. Our results suggest netrin-1 secretion, diffusion, and immobilization on cell surfaces of epithelial and endothelial cells. Taken together, the endothelial localization of netrin-1 as shown in the *in vivo* immuno-localization study, and the reliable detection of cell surface netrin-1 with NET1-H-mAb on endothelial cells, provided our rationale for USMI with netrin-1-targeted UCAs.

In vivo imaging of netrin-1

The *in vivo* USMI study indicated the feasibility of netrin-1 imaging in murine blood vessels supplying human SKBR7 breast tumors in nude mice, and corroborated *in vitro* results of MB binding on breast cancer cell lines. The data confirmed the hypothesis of a correlation between epithelial and endothelial netrin-1 presentation in tumors. Our *in vitro* and *in*

in vivo data show that netrin-1, although described as a secreted and diffusible protein, bound to the cell surface and/or extracellular matrix. This observation is in line with previous reports about USMI of secreted frizzled related protein 2, interleukin 16, and GPIIb/IIIa in tumors, and confirms the feasibility of USMI in settings where free-circulating proteins can potentially saturate MBs and prevent immobilization [22,48,49]. Inter- and intra-tumoral heterogeneity with regard to vascular perfusion rates and functionality of the vascular network are crucial factors for USMI with micrometer-sized contrast agents that are injected and limited to the blood vessels [50,51]. Thus, different tumors might require differently timed injections and imaging protocols to ensure that MBs reach the tumor before and after the destructive pulse, a concept that cannot be translated into practice. Alternatively, one might individually assess tumor heterogeneity and use netrin-1-targeted and isotype control contrast agents to determine background signals and assess the amount of molecular imaging signal in every tumor model. Comparison between MB_{Netrin-1} and MB_{isotype} enabled the reliable detection of netrin-1-positive subcutaneous tumors and confirmed IVIL results. The transgenic MMTV-PyMT mouse model reflects naturally occurring tumor development and neoangiogenesis, critical in USMI, and is more physiologically accurate to human disease than subcutaneously engrafted tumor models, providing clinically relevant insight into imaging of netrin-1 [52]. USMI with both MB_{Netrin-1} and MB_{isotype} enables the reliable detection of netrin-1 expression in MMTV-PyMT breast tumors, and netrin-1 absence in normal mammary glands as confirmed by IVIL analysis. Furthermore, the use of MB_{isotype} revealed that the intensity of background signal differs strongly between the SKBR7 and MDA-MB-231 models so that their netrin-1 molecular imaging signals cannot be directly compared with each other and require the subtraction of background signal. A future challenge will be to reduce baseline signal and amplify signal from bound MBs to facilitate the distinction between netrin-1-positive and negative tumors using netrin-1-targeted MBs only. USMI signal can be normalized by vascularity, which is thought to have an impact on background signal, after estimation of relative blood volume, vessel density, and vessel perfusion [53,54]. The use of three-dimensional USMI might enable more complete assessment of tumor heterogeneity compared to the two-dimensional imaging data of this study, but further technological development is required for a routine use in preclinical or clinical settings [27].

In addition to the characterization of tumor heterogeneity, contrast agents and imaging strategies

can be further developed to overcome tissue-dependent signal variances and produce imaging signals that are solely dependent on the degree of netrin-1 expression: (1) Contrast agents can be prepared by directly integrating/conjugating the targeting moiety to the MB shell, eliminating the need for an immunogenic avidin-biotin bridge. Instead of the whole antibody, which might cause Fc-mediated inadvertent non-specific interactions [55], an antibody Fab fragment or novel targeting peptide has to be prepared to provide a clinically translatable targeted contrast agent that reduces background signal in the tissue. Our blocking studies using NET1-H-mAb IgG, which was expected to bind to netrin-1 and Fc receptors, did not reveal a change in MB_{isotype} imaging signal. Therefore, it was assumed that Fc-mediated binding of NET1-H-mAb did not cause background signal. (2) In this study, MBs were used at a high concentration compared to other studies to increase the sensitivity of our imaging approach for the secreted ligand netrin-1, which was described to be membrane-associated but also free-circulating in the blood. Having shown the feasibility of USMI of netrin-1, a novel study is conceivable in which lower concentrations of MBs can be employed to reduce the level of background signal and facilitate the comparison of heterogeneous tumor models [56]. (3) The imaging protocol based on the destruction-replenishment method has become the standard technique in pre-clinical studies of ultrasound molecular imaging [24]. Though, MB destruction causes cavitation, which potentially harms the blood vessels and affects the comparison of pre- and post-destructive acquisitions [57]. Alternative strategies have been proposed, such as late-phase signal enhancement, which is used in clinical studies [30], and in which images are acquired 30 min after microbubble injection when free-circulating microbubbles are degraded, or techniques based on the microbubble dwell time [58], but they require optimization to allow for fast acquisitions before they can be routinely used.

The diagnostic potential of USMI of netrin-1 was further assessed with ROC curves, which were analyzed with the MB_{Netrin-1} signals of the transgenic MMTV-PyMT tumors and normal mammary glands. ROC curves indicated that USMI of netrin-1 allowed distinction between normal mammary tissue and transgenic tumor endothelium, thus underlining the diagnostic power of the technique.

Conclusion

To the best of our knowledge, this is the first study proposing USMI as a companion diagnostic for a molecularly targeted therapy, thereby promoting

novel targets and applications for USMI. Compared to clinical diagnostics such as immunohistochemistry, USMI is non-invasive, cost efficient, rapid, and can be performed at the point-of-care. In conclusion, after confirmation of netrin-1 presentation on the vascular endothelium of netrin-1-expressing tumors, USMI was successfully developed as a companion diagnostic for this secreted tumor marker. Technical improvements and further pre-clinical therapy response monitoring studies will boost this powerful imaging approach for personalized medicine. The development of USMI for relevant targets can significantly improve the quality of patient management.

Abbreviations

AUC: area under curve; CI: confidence interval; IVIL: *in vivo* immuno-localization; MB: microbubble; MFI: mean fluorescence intensity; MMTV-PyMT: mouse mammary tumor virus polyoma virus middle T antigen; ROC: receiver operating characteristic; SEM: standard error of mean; STD: standard deviation; UCA: ultrasound contrast agent; USMI: ultrasound molecular imaging.

Supplementary Material

Supplementary figures and tables.

<http://www.thno.org/v08p5126s1.pdf>

Acknowledgements

The authors wish to thank Annabelle Bouchardon from the Fédération de Recherche Santé Lyon-Est for assistance with mosaic microscopy and the Laboratoire d'Automatique et de Génie des Procédés (LAGEP) for access to the Zetasizer Nano ZS, Malvern Instruments.

We wish to dedicate our work to our co-author Prof. Dr. Juergen K. Willmann whose death is a profound loss to us and the molecular imaging community.

Funding

This work was supported by the LabEx DEVweCAN (ANR-10-LABX-0061) of the University of Lyon, within the program "Investissements d'Avenir" (ANR-11-IDEX-0007) operated by the French National Research Agency (ANR), the French Ligue nationale contre le cancer, and by NIH R01CA155289 (JKW). The imaging study was performed at the Stanford Center for Innovation in In-Vivo Imaging (SCI³), supported by NIH S10OD010344 for the VisualSonics Vevo2100. Confocal microscopy was performed at the Stanford Neuroscience Microscopy Service, supported by NIH NS069375. The first author, Jennifer Wischhusen, was

supported by the LabEx DEVweCAN (ANR-10-LABX-0061) of the University of Lyon, within the program "Investissements d'Avenir" (ANR-11-IDEX-0007) operated by the French National Research Agency (ANR), by the German-American Fulbright Commission, by the France-Stanford Center for Interdisciplinary Studies, and by NIH R01CA155289.

Author contributions

J.W. planned the study, conducted the experiments, analyzed the data, prepared the figures, and wrote the paper. K.E.W. assisted with experiments and data analysis, and edited the manuscript. J.-G.D. planned experiments, prepared reagents, conducted experiments, analyzed data, and assisted with manuscript writing. R.M.-P. performed experiments. B.G. assisted with experiments and manuscript writing. S.J., J.N., and D.G. performed experiments. P.M. provided funding, and edited the manuscript. J.K.W. helped with planning of experiments and interpretation of data, edited the manuscript, and provided funding. F.P. helped with planning of experiments and interpretation of data, provided funding, performed statistical analyses, and assisted with manuscript writing.

Competing Interests

D. Goldschneider is an employee of Netris Pharma. J.G. Delcros is the inventor of the anti-netrin-1 antibody (patent EP2893939A1). J.G. Delcros and B. Gibert are consultants for Netris Pharma. P. Mehlen is a shareholder of Netris Pharma. The authors J. Wischhusen, K. E. Wilson, R. Molina-Peña, S. Jiang, J. Ngo, and J. K. Willmann, and F. Padilla declare no potential conflicts of interest.

References

- [1] Serafini T, Kennedy TE, Galko MJ, Mirzayan C, Jessell TM, Tessier-Lavigne M. The netrins define a family of axon outgrowth-promoting proteins homologous to *C. elegans* UNC-6. *Cell*. 1994; 78: 409-24.
- [2] Mehlen P, Mazelin L. The dependence receptors DCC and UNC5H as a link between neuronal guidance and survival. *Biol Cell*. 2003; 95: 425-36.
- [3] Mazelin L, Bernet A, Bonod-Bidaud C, Pays L, Arnaud S, Gespach C, et al. Netrin-1 controls colorectal tumorigenesis by regulating apoptosis. *Nature*. 2004; 431: 80-84.
- [4] Park KW, Crouse D, Lee M, Karnik SK, Sorensen LK, Murphy KJ, et al. The axonal attractant Netrin-1 is an angiogenic factor. *Proc Natl Acad Sci USA*. 2004; 101: 16210-16215.
- [5] Fitamant J, Guenebeaud C, Coissieux M-M, Guix C, Treilleux I, Scoazec J-Y, et al. Netrin-1 expression confers a selective advantage for tumor cell survival in metastatic breast cancer. *Proc Natl Acad Sci USA*. 2008; 105: 4850-4855.
- [6] Grandin M, Meier M, Delcros JG, Nikodemus D, Reuten R, Patel TR, et al. Structural decoding of the Netrin-1/UNC5 interaction and its therapeutical implications in cancers. *Cancer Cell*. 2016; 29: 173-185.
- [7] Grandin M, Mathot P, Devaillay G, Bidet Y, Ghantous A, Favrot C, et al. Inhibition of DNA methylation promotes breast tumor sensitivity to netrin-1 interference. *EMBO Mol Med*. 2016; 8: 863-877.
- [8] Xie H, Zou L, Zhu J, Yang Y. Effects of netrin-1 and netrin-1 knockdown on human umbilical vein endothelial cells and angiogenesis of rat placenta. *Placenta*. 2011; 32: 546-553.
- [9] van Gils JM, Ramkhalawon B, Fernandes L, Stewart MC, Guo L, Seibert T, et al. Endothelial expression of guidance cues in vessel wall homeostasis dysregulation under proatherosclerotic conditions. *Arterioscler Thromb Vasc Biol*. 2013; 33: 911-919.

- [10] Passacquale G, Phinikaridou A, Warboys C, Cooper M, Lavin B, Alfieri A, et al. Aspirin-induced histone acetylation in endothelial cells enhances synthesis of the secreted isoform of netrin-1 thus inhibiting monocyte vascular infiltration. *Br J Pharmacol*. 2015; 172: 3548-3564.
- [11] Tu T, Zhang C, Yan H, Luo Y, Kong R, Wen P, et al. CD146 acts as a novel receptor for netrin-1 in promoting angiogenesis and vascular development. *Cell Res*. 2015; 25: 275-287.
- [12] Senkus E, Kyriakides S, Ohno S, Penault-Llorca F, Poortmans P, Rutgers E, et al. Primary breast cancer: ESMO Clinical Practice Guidelines for diagnosis, treatment and follow-up. *Ann Oncol*. 2015; 26 Suppl 5: v8-30.
- [13] Unnikrishnan S, Klivanov AL. Microbubbles as ultrasound contrast agents for molecular imaging: preparation and application. *American Journal of Roentgenology*. 2012; 199: 292-299.
- [14] Kiessling F, Fokong S, Bzyl J, Lederle W, Palmowski M, Lammers T. Recent advances in molecular, multimodal and theranostic ultrasound imaging. *Adv Drug Deliv Rev*. 2014; 72: 15-27.
- [15] Abou-Elkacem L, Bachawal SV, Willmann JK. Ultrasound molecular imaging: Moving toward clinical translation. *Eur J Radiol*. 2015; 84: 1685-1693.
- [16] Pochon S, Tardy I, Bussat P, Bettinger T, Brochot J, von Wronski M, et al. BR55: a lipopeptide-based VEGFR2-targeted ultrasound contrast agent for molecular imaging of angiogenesis. *Invest Radiol*. 2010; 45: 89-95.
- [17] Bettinger T, Bussat P, Tardy I, Pochon S, Hyvelin J-M, Emmel P, et al. Ultrasound molecular imaging contrast agent binding to both E- and P-selectin in different species. *Invest Radiol*. 2012; 47: 516-523.
- [18] Anderson CR, Hu X, Zhang H, Tlaxca J, Declèves A-E, Houghtaling R, et al. Ultrasound molecular imaging of tumor angiogenesis with an integrin targeted microbubble contrast agent. *Invest Radiol*. 2011; 46: 215-224.
- [19] Nakatsuka MA, Barback CV, Fitch KR, Farwell AR, Esener SC, Mattrey RF, et al. In vivo ultrasound visualization of non-occlusive blood clots with thrombin-sensitive contrast agents. *Biomaterials*. 2013; 34: 9559-9565.
- [20] Lutz AM, Bachawal SV, Drescher CW, Pysz MA, Willmann JK, Gambhir SS. Ultrasound molecular imaging in a human CD276 expression-modulated murine ovarian cancer model. *Clin Cancer Res*. 2014; 20: 1313-1322.
- [21] Bachawal SV, Jensen KC, Wilson KE, Tian L, Lutz AM, Willmann JK. Breast Cancer Detection by B7-H3-Targeted Ultrasound Molecular Imaging. *Cancer Res*. 2015; 75: 2501-2509.
- [22] Tsuruta JK, Schaub NP, Rojas JD, Streeter J, Klauber-DeMore N, Dayton P. Optimizing ultrasound molecular imaging of secreted frizzled related protein 2 expression in angiosarcoma. *PLoS ONE*. 2017; 12: e0174281.
- [23] Pysz MA, Foygel K, Rosenberg J, Gambhir SS, Schneider M, Willmann JK. Antiangiogenic cancer therapy: monitoring with molecular US and a clinically translatable contrast agent (BR55). *Radiology*. 2010; 256: 519-527.
- [24] Bachawal SV, Jensen KC, Lutz AM, Gambhir SS, Tranquart F, Tian L, et al. Earlier detection of breast cancer with ultrasound molecular imaging in a transgenic mouse model. *Cancer Res*. 2013; 73: 1689-1698.
- [25] Payen T, Dizeux A, Baldini C, Le Guillou-Buffello D, Lamuraglia M, Comperat E, et al. VEGFR2-Targeted Contrast-Enhanced Ultrasound to Distinguish between Two Anti-Angiogenic Treatments. *Ultrasound Med Biol*. 2015; 41: 2202-2211.
- [26] Baron Toaldo M, Salvatore V, Marinelli S, Palamà C, Milazzo M, Croci L, et al. Use of VEGFR-2 targeted ultrasound contrast agent for the early evaluation of response to sorafenib in a mouse model of hepatocellular carcinoma. *Mol Imaging Biol*. 2015; 17: 29-37.
- [27] Zhou J, Wang H, Zhang H, Lutz AM, Tian L, Hristov D, et al. VEGFR2-targeted three-dimensional ultrasound imaging can predict responses to antiangiogenic therapy in preclinical models of colon cancer. *Cancer Res*. 2016; 76: 4081-4089.
- [28] Baetke SC, Rix A, Tranquart F, Schneider R, Lammers T, Kiessling F, et al. Squamous cell carcinoma xenografts: use of VEGFR2-targeted microbubbles for combined functional and molecular US to monitor antiangiogenic therapy effects. *Radiology*. 2016; 278: 430-440.
- [29] Eschbach RS, Clevert D-A, Hirner-Eppeneder H, Ingrisch M, Moser M, Schuster J, et al. Contrast-enhanced ultrasound with VEGFR2-targeted microbubbles for monitoring regorafenib therapy effects in experimental colorectal adenocarcinomas in rats with DCE-MRI and immunohistochemical validation. *PLoS ONE*. 2017; 12: e0169323.
- [30] Willmann JK, Bonomo L, Carla Testa A, Rinaldi P, Rindi G, Valluru KS, et al. Ultrasound molecular imaging with BR55 in patients with breast and ovarian lesions: first-in-human results. *J Clin Oncol*. 2017; 35: 2133-2140.
- [31] Smeenge M, Tranquart F, Mannaerts CK, de Reijke TM, van de Vijver MJ, Laguna MP, et al. First-in-human ultrasound molecular imaging with a VEGFR2-specific ultrasound molecular contrast agent (BR55) in prostate cancer: a safety and feasibility pilot study. *Invest Radiol*. 2017; 52: 419-427.
- [32] Wilson KE, Bachawal SV, Abou-Elkacem L, Jensen K, Machtaler S, Tian L, et al. Spectroscopic photoacoustic molecular imaging of breast cancer using a B7-H3-targeted ICG contrast agent. *Theranostics*. 2017; 7: 1463-1476.
- [33] Cardiff RD. Validity of mouse mammary tumour models for human breast cancer: comparative pathology. *Microsc Res Tech*. 2001; 52: 224-230.
- [34] Mach JP, Chatal JF, Lumbroso JD, Buchegger F, Forni M, Ritschard J, et al. Tumor localization in patients by radiolabeled monoclonal antibodies against colon carcinoma. *Cancer Res*. 1983; 43: 5593-5600.
- [35] Juweid M, Neumann R, Paik C, Perez-Bacete MJ, Sato J, van Osdol W, et al. Micropharmacology of monoclonal antibodies in solid tumors: direct experimental evidence for a binding site barrier. *Cancer Res*. 1992; 52: 5144-5153.

- [36] Eccles SA, Purvies HP, Styles JM, Hobbs SM, Dean CJ. Pharmacokinetic studies of radiolabelled rat monoclonal antibodies recognising syngeneic sarcoma antigens. II. Effect of host age and immune status. *Cancer Immunol Immunother.* 1989; 30: 13–20.
- [37] Netti PA, Hamberg LM, Babich JW, Kierstead D, Graham W, Hunter GJ, et al. Enhancement of fluid filtration across tumor vessels: implication for delivery of macromolecules. *Proc Natl Acad Sci USA.* 1999; 96: 3137–3142.
- [38] Maeda H, Wu J, Sawa T, Matsumura Y, Hori K. Tumor vascular permeability and the EPR effect in macromolecular therapeutics: a review. *Journal of Controlled Release.* 2000; 65: 271–284.
- [39] Prabhakar U, Maeda H, Jain RK, Sevick-Muraca EM, Zamboni W, Farokhzad OC, et al. Challenges and key considerations of the enhanced permeability and retention effect for nanomedicine drug delivery in oncology. *Cancer Res.* 2013; 73: 2412–2417.
- [40] Schindelin J, Arganda-Carreras I, Frise E, Kaynig V, Longair M, Pietzsch T, et al. Fiji: an open-source platform for biological-image analysis. *Nat Methods.* 2012; 9: 676–682.
- [41] Wischhusen J, Padilla F. Microbubble enzyme-linked immunosorbent assay for the detection of targeted microbubbles in *in vitro* static binding assays. *Ultrasound Med Biol.* 2017; 43: 1506–1519.
- [42] Deshpande N, Ren Y, Foygel K, Rosenberg J, Willmann JK. Tumor angiogenic marker expression levels during tumor growth: longitudinal assessment with molecularly targeted microbubbles and US imaging. *Radiology.* 2011; 258: 804–811.
- [43] El Kaffas A, Smith K, Pradhan P, Machtaler S, Wang H, von Eyben R, et al. Molecular contrast-enhanced ultrasound imaging of radiation-induced P-selectin expression in healthy mice colon. *Int J Radiat Oncol Biol Phys.* 2017; 97: 581–585.
- [44] Willmann JK, Cheng Z, Davis C, Lutz AM, Schipper ML, Nielsen CH, et al. Targeted microbubbles for imaging tumor angiogenesis: assessment of whole-body biodistribution with dynamic micro-PET in mice. *Radiology.* 2008; 249: 212–219.
- [45] Castets M, Coissieux M-M, Delloye-Bourgeois C, Bernard L, Delcros J-G, Bernet A, et al. Inhibition of endothelial cell apoptosis by Netrin-1 during angiogenesis. *Dev Cell.* 2009; 16: 614–620.
- [46] Dudley AC. Tumor endothelial cells. *Cold Spring Harb Perspect Med.* 2012; 2: a006536.
- [47] Moon JJ, Matsumoto M, Patel S, Lee L, Guan J-L, Li S. Role of cell surface heparan sulfate proteoglycans in endothelial cell migration and mechanotransduction. *J Cell Physiol.* 2005; 203: 166–176.
- [48] Barua A, Yellapa A, Bahr JM, Adur MK, Utterback CW, Bitterman P, et al. Interleukin 16- (IL-16-) targeted ultrasound imaging agent improves detection of ovarian tumors in laying hens, a preclinical model of spontaneous ovarian cancer. *Biomed Res Int.* 2015; 2015:567459.
- [49] Yap ML, McFadyen JD, Wang X, Zia NA, Hohmann JD, Ziegler M, et al. Targeting activated platelets: a unique and potentially universal approach for cancer imaging. *Theranostics.* 2017; 7: 2565–2574.
- [50] Kiessling F, Boese J, Corvinus C, Ederle JR, Zuna I, Schoenberg SO, et al. Perfusion CT in patients with advanced bronchial carcinomas: a novel chance for characterization and treatment monitoring? *Eur Radiol.* 2004; 14: 1226–1233.
- [51] Palmowski M, Schifferdecker I, Zwick S, Macher-Goeppinger S, Laue H, Haferkamp A, et al. Tumor perfusion assessed by dynamic contrast-enhanced MRI correlates to the grading of renal cell carcinoma: initial results. *Eur J Radiol.* 2010; 74: e176–180.
- [52] Fantozzi A, Christofori G. Mouse models of breast cancer metastasis. *Breast Cancer Res.* 2006; 8: 212–223.
- [53] Pitre-Champagnat S, Leguery I, Bosq J, Peronneau P, Kiessling F, Calmels L, et al. Dynamic contrast-enhanced ultrasound parametric maps to evaluate intratumoral vascularization. *Invest Radiol.* 2015; 50: 212–217.
- [54] Zafarnia S, Bzyl-Ibach J, Spivak I, Li Y, Koletnik S, Doleschel D, et al. Nilotinib enhances tumor angiogenesis and counteracts VEGFR2 blockade in an orthotopic breast cancer xenograft model with desmoplastic response. *Neoplasia.* 2017; 19: 896–907.
- [55] Datta-Mannan A, Lu J, Witcher DR, Leung D, Tang Y, Wroblewski VJ. The interplay of non-specific binding, target-mediated clearance and FcRn interactions on the pharmacokinetics of humanized antibodies. *MABs.* 2015; 7: 1084–1093.
- [56] Wang S, Herbst EB, Mauldin FW, Diakova GB, Klivanov AL, Hossack JA. Ultra-low-dose ultrasound molecular imaging for the detection of angiogenesis in a mouse murine tumor model: how little can we see? *Invest Radiol.* 2016; 51: 758–766.
- [57] Lentacker I, De Cock I, Deckers R, De Smedt SC, Moonen CTW. Understanding ultrasound induced sonoporation: definitions and underlying mechanisms. *Adv Drug Deliv Rev.* 2014; 72: 49–64.
- [58] Pysz MA, Guracar I, Tian L, Willmann JK. Fast microbubble dwell-time based ultrasonic molecular imaging approach for quantification and monitoring of angiogenesis in cancer. *Quant Imaging Med Surg.* 2012; 2: 68–80.